Gen Satoh
Department of Mechanical Engineering,
Columbia University,
New York, NY 10023
e-mail: gs2385@columbia.edu

Grant Brandal[1]
Department of Mechanical Engineering,
Columbia University,
500 West 120th Street,
Mudd Rm 220,
New York, NY 10023
e-mail: gbb2114@columbia.edu

Syed Naveed
Endoscopy Division,
Boston Scientific Corporation,
Marlborough, MA 01752
e-mail: syed.naveed@bsci.com

Y. Lawrence Yao
Fellow ASME
Department of Mechanical Engineering,
Columbia University,
New York, NY 10023
e-mail: yly1@columbia.edu

Laser Autogenous Brazing of Biocompatible, Dissimilar Metals in Tubular Geometries

The successful joining of dissimilar metal tubes would enable the selective use of the unique properties exhibited by biocompatible materials such as stainless steel and shape memory materials, such as NiTi, to locally tailor the properties of implantable medical devices. The lack of robust joining processes for the dissimilar metal pairs found within these devices, however, is an obstacle to their development and manufacture. Traditional joining methods suffer from weak joints due to the formation of brittle intermetallics or use filler materials that are unsuitable for use within the human body. This study investigates a new process, Laser Autogenous Brazing, that utilizes a thermal accumulation mechanism to form joints between dissimilar metals without filler materials. This process has been shown to produce robust joints between wire specimens but requires additional considerations when applied to tubular parts. The strength, composition, and microstructure of the resultant joints between NiTi and stainless steel are investigated and the effects of laser parameters on the thermal profile and joining mechanism are studied through experiments and numerical simulations. [DOI: 10.1115/1.4035034]

Introduction

The joining of dissimilar metals is of great interest to the field of engineering due to the need for enhanced performance and decreased weight and cost in a wide range of parts and devices. These requirements drive the desire for the use of specific materials in selective and localized areas of a part. While straightforward applications of this concept have been realized and are enjoying great success in industry, these applications, such as tailor-welded blanks in the automotive industry, are generally concerned with joining similar types of metals such as high-strength steel to mild steel [1]. A greater degree of difficulty is encountered when joining materials with vastly different compositions and properties due to the greater possibility of the formation of brittle intermetallic phases as well as thermo-mechanical differences such as thermal expansion coefficients, which lead to stresses within the dissimilar metal joint. These issues keep the majority of dissimilar metals from being joined by traditional joining methods.

In addition to the inherent issues faced by all dissimilar metal joining processes, joining features at the microscale introduce further difficulties largely due to the lack of precision in thermal input and joint morphology in macroscale joining processes. Many processes rely on global temperature increases in a furnace [2] or the application of extreme forces during ultrasonic agitation [3,4]. These processes do not translate to many microscale applications, which require significantly higher dimensional precision and minimal and localized thermal input to protect heat-sensitive components. Requirements for joining dissimilar metals in the microscale are often encountered in the medical device industry where materials such as shape memory alloys (SMAs) and noble metals, in the form of Nickel–Titanium (NiTi) and Platinum, are used for their unique mechanical and thermo-mechanical properties, radiopacity, and biocompatibility. The geometry of many parts in implantable medical devices and instruments causes additional constraints on the joining process. The use of tubular geometries is governed by the need to pass fluids and/or other devices through the lumen. Examples include stents and catheters. The joining of tubes for these purposes, with their wall thicknesses being only hundreds of microns thick, requires even greater precision in the joining process.

A number of methods for joining dissimilar materials have been developed in order to overcome the formation of brittle intermetallics. The addition of an interlayer, which acts as a barrier between the two materials to be joined, is a popular option due to the relative ease of manufacture and availability of suitable filler materials, such as silver, that do not readily form intermetallics with typical base materials. However, the strength of the interlayer materials, as well as their biocompatibility, is still a major concern. Filler materials are typically made of lower melting temperature materials, which limit the working temperature of the joined part and typically are correlated with lower strength. Diffusion bonding of dissimilar metal pairs with and without interlayers has been investigated by Ghosh and Chatterjee [5] and Kundu and Chatterjee [6] with some success but requires the application of a substantial stress to the items to be joined and heating of the entire part. Campbell et al. has shown the ability to form solid joints between dissimilar metal pairs with an interlayer through transient liquid-phase bonding where joining can occur at a constant temperature [7]. This method, however, relies on the existence of a melt-temperature depressant that can diffuse into the base materials upon heating, thus increasing the solidus temperature leading to solidification.

Localization of the thermal input for joining of microscale parts can be achieved by laser irradiation with its highly localized beam and precise thermal input. Vannod et al. have performed laser fusion welding of the NiTi–SS dissimilar metal pair [8]. While these joints have shown reasonable strength, as expected from fusion welding processes, the width of the joint is large, resulting in a widespread elimination of shape memory properties surrounding the joint. The authors have recently developed a new process, autogenous laser brazing, for joining dissimilar metal pairs and showed the capability to join 381 μm diameter NiTi and stainless steel wires in a butt joint geometry [9]. This process takes

[1]Corresponding author.

Manuscript received December 3, 2015; final manuscript received October 10, 2016; published online November 10, 2016. Assoc. Editor: Hongqiang Chen.

advantage of the thermal accumulation that occurs at the dissimilar metal interface prior to joining to produce a localized braze-like joint between the two materials. Joint widths have been shown to reach the micrometer length scale using this process due to the localization of thermal accumulation at the dissimilar metal interface.

In this study, the autogenous laser brazing process is adapted to the joining of NiTi and stainless steel in tubular geometries. The resultant structural and thermal constraints are expected to require significant modifications to the joining process. Laser joining experiments are performed and the resultant strength is determined through tensile testing while microstructural analysis is performed using optical microscopy (OM) and scanning electron microscopy (SEM). Compositional information is provided by energy-dispersive X-ray spectroscopy (EDS) and electron backscatter diffraction (EBSD). Further understanding of the joining mechanism for tubular samples is gained through thermal and microstructural numerical simulations.

Background

Laser Autogenous Brazing Process. In order to mitigate the formation of intermetallics in dissimilar metal joining, the authors have developed a new process, Autogenous Laser Brazing, to form joints between dissimilar metal pairs without a filler material [9]. This process takes advantage of the imperfect thermal contact between the two faying surfaces before the joint is formed. A laser beam is used to precisely irradiate one side of the joint while scanning toward the interface. As the laser approaches the interface, the reduction of conduction pathways from the beam spot causes a greater amount of thermal accumulation to occur, causing the temperature to rise. The softened or molten material then comes into intimate contact with the adjacent solid part, which is still relatively cool. This causes rapid quenching of the irradiated material and minimizes the amount of mixing between the two dissimilar materials.

Through-thickness joining at the interface requires that the temperature profile on the irradiated member's faying surface be uniform. The thermal diffusivity of the material must be high enough such that there is not an appreciable difference in temperature between the top, irradiated, surface of the member and its interior. The strength of the temperature gradient formed in a sample under scanning laser irradiation can be described by the Fourier number which is written as

$$F = \frac{\alpha D}{v {s_o}^2} \tag{1}$$

where $\alpha = k/\rho c_p$ is the thermal diffusivity, D is the laser beam diameter, v is the scan speed, and s_o is the material thickness. Through-thickness thermal gradients are expected to form for cases where the Fourier number is much less than unity. This is caused by the interaction time with the laser being much shorter than the time required for thermal diffusion. The tubular geometry of the samples used in this study further increases temperature gradients compared to wires, due to the lack of a direct conduction pathway across the interior. Rotation of the tubular samples about their longitudinal axis, however, allows for direct irradiation around the entire circumference. Thus, s_o becomes the wall thickness rather than the tube diameter. This allows for higher scan speeds for the same Fourier number and minimal thermal gradients in the circumferential direction.

Since large-scale deformation during joining is undesirable due to the need to maintain part geometry, the temperature of the material should be kept below the melting temperature for the majority of the irradiated region. An axial force is provided to the parts to be joined during the autogenous laser brazing process to promote wetting and quenching of the irradiated material on the adjacent, nonirradiated surface.

Diffusion in Dissimilar Metal Pairs. In any joining process involving metals at elevated temperatures, diffusion is likely to occur, whether intended or not. In the case of joining similar materials, this diffusion is accepted and even encouraged in order to create a seamless joint. In the case of dissimilar metal joints where intermetallics are expected to form, however, the diffusion of materials across the interface must be minimized. As discussed above, one method to mitigate these effects is to eliminate the possibility of diffusion through the use of a diffusion barrier or interlayer coating. These layers are applied to one or both of the faying surfaces prior to joining and keep the base materials separated during and after joining. The other method, which is used during the autogenous laser brazing process, is to restrict the maximum temperature achieved in the parts as well as the duration of heating to control the total diffusive transport across the interface.

The diffusive transport between two materials during a thermal cycle can be described as a diffusion couple. The two materials are initially separate with different uniform compositions. Diffusion is allowed to occur across the interface with the diffusion coefficient following the Arrhenius relationship defined as

$$D_{\mathrm{ef}} = D_{\mathrm{ef}}^{o} \exp\left(-Q_{\mathrm{ef}}/RT\right) \tag{2}$$

where Q_{ef} is the activation energy, R is the gas constant, T is temperature, and ${D_{\mathrm{ef}}}^{o}$ is the interdiffusion coefficient.

The existence of intermetallics, which have a limited homogeneity range, complicates diffusive transport in these material systems since the chemical potential at different compositions varies considerably. Even with a purely diffusion-based joining process, constant composition regions are expected to form at the intermetallic compositions [10]. The width of an intermetallic layer, Δx, formed during diffusion in a diffusion couple at a constant temperature can be estimated by the parabolic growth law [11]

$$\Delta x = k_o t^n \tag{3}$$

where k_o is the parabolic growth constant, t is time, and n is nominally 0.5.

While diffusion has a large role in determining the resultant composition profile across a dissimilar metal joint, at higher temperatures caused by slower scanning and greater laser power, fluid flow may control the joint formation mechanism, final phases, and microstructure.

Fracture Toughness. While fracture toughness is easily measured in macroscopic samples due to the ability to impart cracks of known geometries and lengths, these methods produce little-to-no spatial resolution due to the large size of the crack. Thus, for samples with locally varying material properties, a method to produce smaller cracks that will be confined to within those local variations must be implemented. This requirement is met through the use of nanoindentation for fracture toughness measurements. With sufficient load applied to an indenter, cracks can be generated which often emanate radially from the corners of the indentation. The hoop stress resulting from the formation of the plastically deformed region under the indenter can be described as [12]

$$\sigma_{\mathrm{hoop}} = \frac{2\gamma}{r^3}\frac{E}{H} - \frac{P}{4\pi r^2} \tag{4}$$

where γ is a parameter dependent on the indenter geometry, r is the radial distance from the center of the indenter, E and H are the modulus and hardness of the material, and P is the load on the indenter. This stress is responsible for the propagation of radial cracks. The resultant radial crack length from the center of the indentation is measured subsequent to indentation and combined with material properties derived from the nanoindentation load–displacement data to determine the fracture toughness. The fracture toughness, K_c, of a material is described by Pharr et al. [12] as

$$K_c = \alpha\left(\frac{E}{H}\right)^{1/2}\left(\frac{P}{c^{3/2}}\right) \tag{5}$$

where E, H, P, and c are the material's modulus and hardness, the indentation load, and the radial crack size, respectively. α is an empirical constant which depends on the geometry of the indenter tip whether it is a Berkovich, Vickers, cube corner, or other geometry. The spatial resolution allowed by performing small indentations can reach submicron levels with greater spatial resolution achievable with sharper indentations due to the greater residual hoop stress introduced by sharper indenter geometry for the same contact area. An α value of 0.032 is used in the current analysis as described by Pharr et al. [12] for a cube-corner indenter geometry.

Numerical Simulation. *Thermal:* A three-dimensional Fourier heat transfer model is used in order to determine the thermal profiles in time and space existing within the tubes during the autogenous laser brazing process. The finite element mesh on the tubes consists of quadratic heat transfer elements with mesh density biased toward the joint interface. The laser irradiation is input as a heat flux on the outer surface of the tubes following a Gaussian spatial distribution, which is translated in a helical pattern by applying a coordinate transformation to the nodes on the tube surface. The conductance across the interface between the two tubes is directed to change, irreversibly, from a low value indicative of two rough surfaces in contact, to the conductance of the NiTi base material, at the melting temperature of NiTi, 1583 K.

Convective cooling of the material is included through the use of a heat transfer coefficient and a sink temperature of 300 K. The heat transfer coefficient is determined through the use of the Zhukauskas relation for flow over a cylinder

$$\overline{\mathrm{Nu}}_D = C\mathrm{Re}_D^m\mathrm{Pr}^n(\mathrm{Pr}/\mathrm{Pr}_s)^{1/4} \tag{6}$$

where m and C are constants dependent on the Reynolds number, Pr is the Prandtl number, n is a constant of 0.37 for $\mathrm{Pr} <= 10$, and Pr_s is the Prandtl number calculated at the surface temperature. The cross-flow velocity of Argon across the tubes is calculated using the flow rate and the cross-sectional area of the argon box. The effect of the tube spinning results in a surface velocity much smaller than that due to the Argon flow and is thus neglected. The convective heat transfer coefficient resultant from the Argon flow is thus calculated to be on the order of 600 $\mathrm{W/m^2/K}$.

Grain Growth: The resultant grain size due to the thermal profile experienced by the material is predicted using a spatially resolved Monte Carlo grain growth simulation as described by the authors in a previous work [13]. In this case, the simulation is used to determine grain growth through solid-phase thermal treatment rather than epitaxial growth. Thus, a new scaling factor between the number of completed Monte Carlo steps (MCS) and time must be determined. The scaling factor used in this study follows Raabe [14] such that:

$$\Delta t_{\mathrm{real}} = \frac{\lambda_p}{\Delta t_{\mathrm{MC}} m_o p} e^{\frac{Q_{gb}}{k_b T}} \tag{7}$$

where Δt_{real} is the time duration in seconds, λ_p is the width of a single element in the Monte Carlo model, Δt_{MC} is the number of Monte Carlo Steps, m_o is the pre-exponential factor to the mobility, p is the driving force for grain boundary motion, Q_{gb} is the activation energy for grain boundary mobility, k_b is Boltzmann's constant, and T is temperature. m_o is calculated as

$$m_o = \frac{\nu b \Omega}{k_b T} \tag{8}$$

where ν is the Debye frequency, b is the length of the Burgers vector, and Ω is the atomic volume. For $\Delta t_{\mathrm{mc}} = 1$, Δt_{real} represents the time duration represented by a single MCS as a function of temperature. The spatial resolution of the Monte Carlo simulation used in this model is 1.33 μm. Q_{gb} is set to equal the activation energy of self-diffusion. Using this scaling factor, the total number of MCS required to simulate grain growth for a specific temperature time history can be calculated as

$$\mathrm{MCS} = \int_0^t \frac{t\Delta t_{\mathrm{MC}} m_o p}{\lambda_p} e^{\frac{-Q_{\mathrm{gb}}}{k_b T}} dt \tag{9}$$

For this study, since the grain growth is expected to occur in the solid state for the majority of the laser parameters, the energy for each node in the Monte Carlo model is based only on the number of interfaces as determined by the number of nearest neighbors with a different crystal orientation. The effects of surface energy used in the previous work for epitaxial growth are removed for this analysis.

Experimental Setup. NiTi and Stainless Steel 304 tubes with respective inner diameters of 940 μm and 870 μm and outer diameters of 1064 μm were cut to two inch lengths for joining. The ends of the tubes were ground flat and perpendicular to the tube axis using 800-grit Silicon Carbide grinding paper. Ultrasonic cleaning was performed in an Acetone bath followed by drying by compressed air. The two dissimilar tube samples were aligned in a butt-joint configuration on a three-axis stage system consisting of an XY linear translation stage and a horizontal rotary axis. The tube to be irradiated was mounted in a chuck on the rotary stage and the second tube is aligned concentrically with the first and is held by bearings to allow for free rotation. Rotation is constant at a speed of 3600 deg/s. An axial force is applied to the nondriven tube through a weight to ensure consistent and repeatable force application. Inert gas shielding is provided by Argon flow into a box surrounding the joint at a flow rate of 10 cfh.

Irradiation of the tubes is performed with a fiber laser with a maximum power output of 20 W at the 1064 nm wavelength. Laser spot size is 900 μm, and the linear scan rate along the axial direction is 0.25 mm/s. Laser firing is synchronized with the stage motion allowing for consistent laser scan paths. Processing was performed using continuous-wave (CW) laser irradiation. A schematic diagram of the experimental setup and laser scan path are shown in Fig. 1.

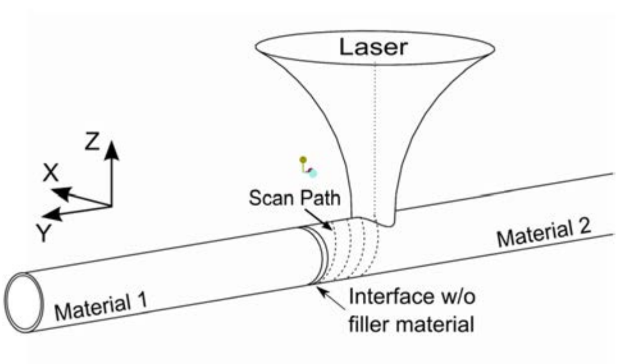

Fig. 1 Schematic diagram of laser processing setup for tube joining. Note helical laser scan path to promote temperature uniformity at the joint interface.

Results and Discussion

Joint Geometry. Figure 2 shows an optical micrograph of a NiTi–stainless steel dissimilar metal joint as formed by the autogenous laser brazing process. Oxidation caused by the heating

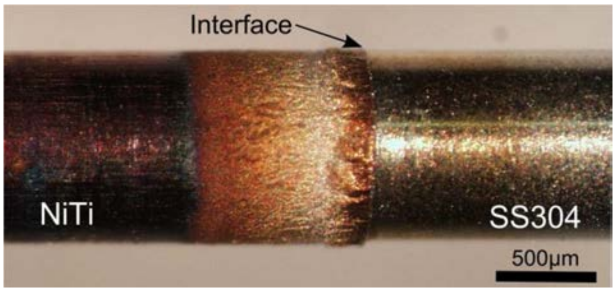

Fig. 2 Optical micrograph of typical joint produced between NiTi and stainless steel tubes through the autogenous laser brazing process. Note discoloration on outer surface of NiTi tube due to oxidation.

cycle, observed as a color change, is found locally around the joint interfaces and is limited primarily to the NiTi side of the joint. This oxidation will influence the biocompatibility, and as such should be minimized. No evidence of melting or deformation of the stainless steel tube is observed on its outer surface. This indicates that the majority of the laser interaction and temperature rise was experienced by the irradiated tube as desired to minimize diffusion and/or other mass transport across the dissimilar metal interface. Some deformation of the geometry is induced, evidenced by the increase in the outer diameter of the NiTi tube adjacent to the joint. This deformation is more pronounced for samples irradiated under higher laser powers due to excessive softening/melting resulting in buckling and collapse of the original tubular geometry. At the lower power levels, no evidence of large-scale melting of the NiTi side of the joint is observed. Samples irradiated at higher power levels do show evidence of melting in so much as they possess smooth outer surface morphologies where laser irradiation occurred with evidence of some fluid flow in the solidified geometry. Each helical laser scan can also be observed in the surface morphology.

Figure 3 shows EDS maps of samples irradiated at two different power levels after cross sectioning and polishing. It is observed that the thickness of the NiTi tube walls increases in the irradiated portion due to softening of the material during irradiation and the application of an axial force. The sample irradiated at lower power, Fig. 3(*a*), shows a modest increase in thickness, allowing the thinner NiTi tube wall to nearly match the thickness of the SS tube wall at the interface. The sample irradiated at higher power, Fig. 3(*b*), experiences excessive deformation and thickening of the tube wall at the joint resulting in a NiTi wall thickness greater than that of the SS. This has the effect of increasing the overall joining area for samples irradiated at higher powers and the resultant strength of the joints must be viewed in light of this increased surface area.

The cross sections also indicate that joining was achieved across the majority of the thickness of the NiTi tube wall for both laser powers. The lumen of the tubes, which must remain clear after joining, is also not significantly impinged upon by the displaced material.

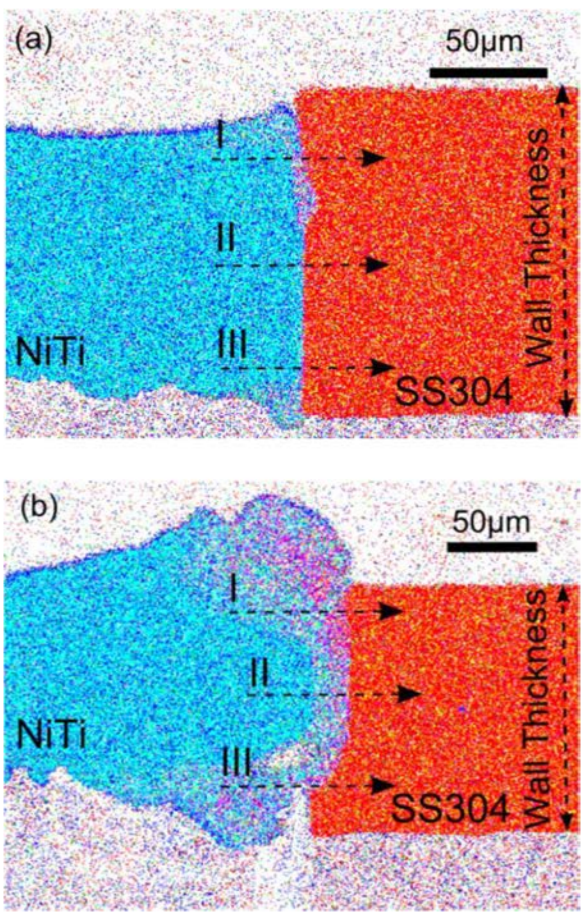

Fig. 3 EDS maps of tube wall after cross sectioning on YZ-plane for laser powers of (*a*) 13 W and (*b*) 15.2 W. Note greater deformation for higher power processing. Red on the rectangular right-hand side represents Fe, while the deformed left-hand side has blue and green for Ti and Ni, respectively.

Joint Composition. The EDS color maps in Fig. 3 also describe the mixing between materials occurring during the joining process. In each figure, Fe, Ni, and Ti are represented by red, green, and blue coloring, respectively. The NiTi sides of the joints are a uniform green/blue coloring and the SS portion has red coloring. The interfaces between the two regions for the two laser power levels, however, are starkly different. At lower laser power, the interface is delineated by a sharp change in the composition. Some regions along the interface show some signs of greater mixing but the joint width is narrow relative to the tube wall thickness. At the higher power level shown in Fig. 3(*b*), the region with mixed red/green/blue coloring is significantly wider and nonuniform with the narrowest region occurring at the midpoint of the wall thickness. The mixed region is also observed to extend past the original interface position into the SS tube material. This suggests that, at the higher power levels, melting of the SS-side of the joint does occur. This is undesirable due to the added mixing occurring for such samples which is expected to result in the formation of a greater volume of brittle intermetallic phases. Figure 4(*a*) shows the atomic fractions of Fe, Ni, Ti, and Cr across the joint interface following the path depicted in Fig. 3(*a*). The overall profile across the interface indicates a diffusion-dominated joining mechanism with its monotonic, sigmoid-shaped composition contour across the interface. Joints that are formed through a melt-dominated process between the same materials have shown the layer between the base materials to be a nearly constant composition due to the strong mixing caused by Marangoni convection within the melt pool [9]. No evidence of such constant composition region is observed in these profiles.

Figure 4(*b*) shows a composition profile across a joint that was formed at a higher laser power of 15.2 W. The profiles show a significantly wider mixed zone between the two base materials with large oscillations across its width. Some evidence of constant-composition regions within the mixed zone is observed, such as the region between 38 μm and 42 μm positions. This could be caused by two different mechanisms, either melting or long-term diffusion in the solid state. As described above, with intermetallic phases with narrow homogeneity ranges expected to form in a Ni-Ti-Fe mixture, diffusive mass transport across the interface will cause the formation of constant-composition regions within the mixed layer. The width of these regions is a function of the temperature profile in time as described in Eq. (3). For higher

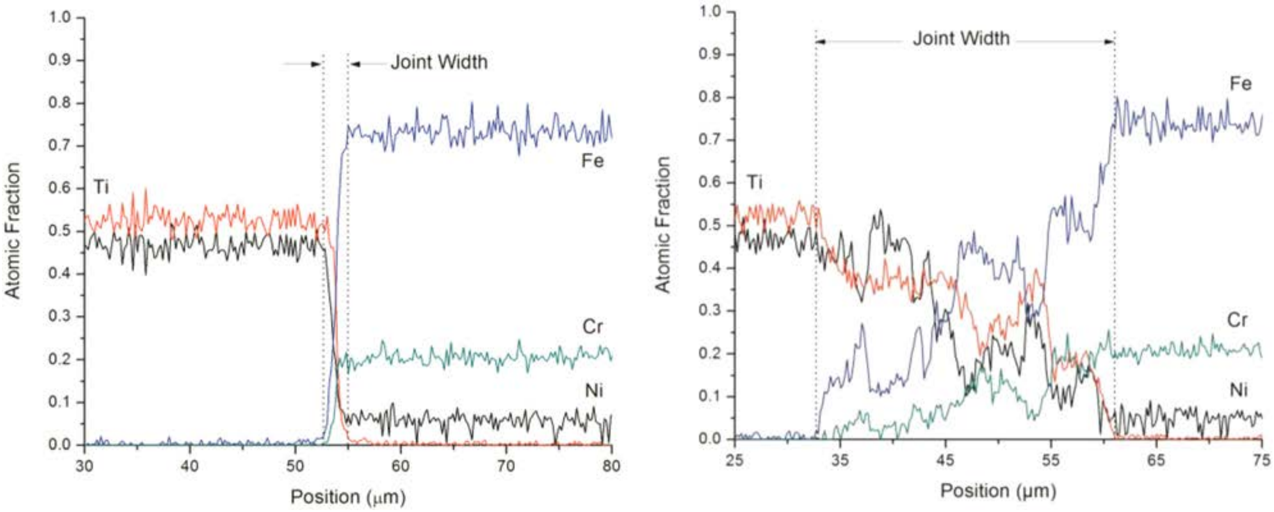

Fig. 4 EDS line scans across joint interface for samples irradiated at (*a*) 13 and (*b*) 15.2 W. Scanning was performed in the middle of the joint, on line II indicated in Figs. 3(*a*) and 3(*b*).

temperatures and longer processing times, the width of the intermetallic layer is expected to increase. The frequent and large oscillations in the composition profiles across the mixed zone, however, indicate that a mechanism beside diffusion, which would result in a monotonic change in composition across the interface, is responsible for the mixing at these higher laser powers. It is believed that the composition profiles are a result of a combination of diffusion and high-temperature deformation.

Figure 5 shows the width of the mixed zone observed at the interface as measured by EDS line profiles as a function of applied laser power. The overall width is seen to increase as a function of laser power except at the highest laser power. For the lowest power levels, no evidence of large-scale melting of the tube walls is observed in the microstructure. This suggests that the layers are formed in a diffusion-based mechanism. The thickness of the joint is also observed to be nearly constant along the wall thickness of the tubes. This is expected since, for the parameters considered in this study, the Fourier number as calculated from Eq. (1) suggests that there will be a negligible temperature gradient across the wall thickness. The significant differences in joint thickness for the high-power irradiated samples are considered to be due to deformation of the softened, mixed material rather than inhomogeneous temperature profile across the wall thickness.

Thermal: With the narrow homogeneity ranges of the intermetallic phases expected to form in a Ni-Ti-Fe mixture, the formation of these phases is nearly guaranteed at elevated temperature and even short-time durations. Equation (3) describes the width of the intermetallic layers as a function of the thermal profile in time, which can be determined through numerical simulation of the joining process. Figure 6 shows a temperature color contour map of the two tubes during irradiation from the numerical simulation. A sharp drop in temperature is observed across the dissimilar metal interface before joining due to the low thermal conductivity across the interface. The temperature uniformity in the circumferential direction is high due to the high rotation rate and large laser beam diameter, which is roughly equal to the tube diameter. In addition, as predicted by the Fourier number as described by Eq. (1), there is a minimal temperature gradient across the thickness of the tube wall. Figure 7 shows the temperature time histories of a number of points different distances away from the interface. Oscillation of the temperature is observed to the greatest extent in locations where direct irradiation by the laser occurs and is caused by the laser passing that point periodically due to the rotation of the tube. Points closer to the start of the laser scan path experience overall lower maximum temperatures that occur earlier during the processing due to the reduced time for heat accumulation by the time the laser reaches that location. The maximum temperature is

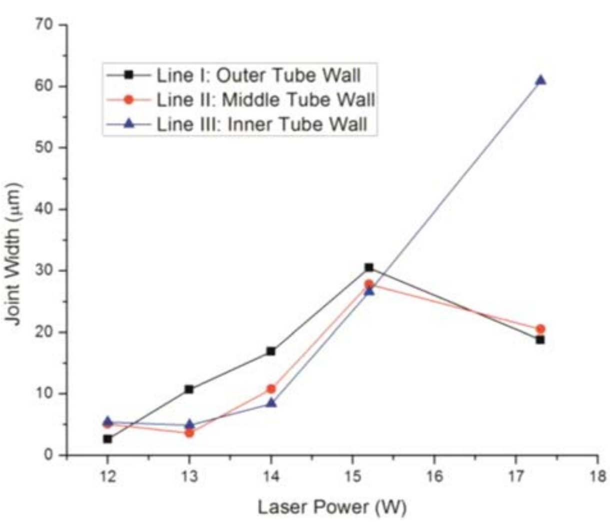

Fig. 5 Joint width versus laser power as measured from EDS line scans. Line numbers correspond to those indicated in Figs. 3(*a*)–3(*b*).

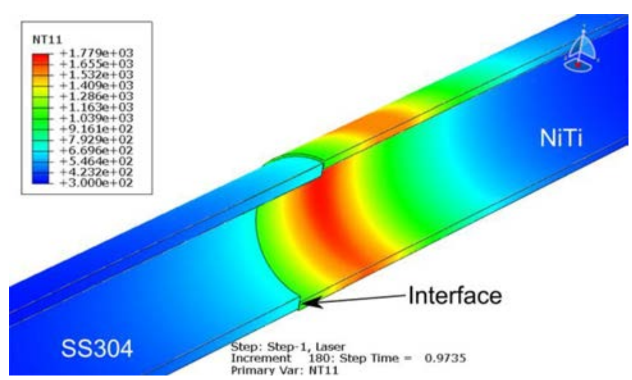

Fig. 6 Thermal contours during laser processing from numerical simulation. Simulated geometry cross sectioned along *YZ*-plane for clarity. Note sharp drop in temperature across interface prior to joining.

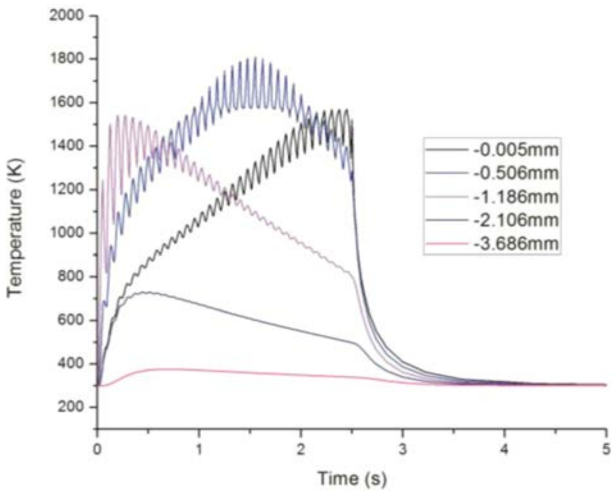

Fig. 7 Simulated temperature time histories from nodes at different distances away from the joint interface along the irradiated tube surface. Oscillation in temperature due to rotation of sample under laser beam.

also seen to be nonmonotonic with points near the center of the irradiated region experiencing the highest temperatures and the beginning and ends of the laser scan path reaching lower temperatures. While the points close to the start of the scan path will reach a lower temperature due to the shorter duration of laser interaction by the time the laser reaches those points, for points at the end of the laser scan path, the tube will have experienced the greatest duration of heating by the time they are reached. The lower maximum temperature at the interface is likely due to the quenching effect from the adjacent SS tube. The current thermal model switches the gap conductance at the melting temperature of NiTi. For the current set of parameters, the interface nodes reach this temperature before the laser has reached that position. Thus, while thermal accumulation due to the low gap conductance is active during the initial stages of laser scanning, by the time the laser has reached the end of its path, the joining and quenching have already occurred.

Grain Growth. Figures 8(*a*)–8(*c*) show portions of the cross sections (*YZ*-plane) of a sample joined by autogenous laser brazing different distances away from the joint interface after etching by Kroll's reagent. As revealed by the etching, the overall grain size of the NiTi is observed to increase in the irradiated region due to the high temperatures experienced during processing. The base NiTi tube has a grain size of roughly 8 μm, which increases to a maximum of roughly 30 μm close to the joint interface. The majority of the grain growth is confined to the irradiated region with some growth occurring to areas not directly affected by the laser. Figure 9 shows grain size as a function of distance from the joint interface for samples irradiated at two different laser powers. The two curves show that grain growth does extend past the laser start position to the unirradiated material and that the grain size closer to the laser start point is quite similar for the two laser powers. More significant changes in grain size, however, are observed as the joint interface is approached. For lower laser powers, the grain size decreases at the interface while for the higher laser power, the grain size continues to increase. This difference in distribution is considered to be caused by the difference in thermal energy stored in the materials. For low laser powers, the peak temperature will be lower along the entire irradiated path. This heat can be quickly dissipated once the joint is formed to the comparatively cool SS tube. For the higher power sample, overheating of the NiTi material occurs, resulting in slower quenching of the material upon contact with the SS.

Grain Growth: The number of Monte Carlo steps (MCS) required to simulate grain growth as a function of distance from the joint interface can be determined from Eq. (7) which includes considerations for the temperature time histories at each node. Due to the higher maximum temperature occurring farther from the joint interface, the number of MCS required to model the grain growth in those regions is higher. Figure 10 shows the grain size estimated by the Monte Carlo model as well as the experimental results for the same laser parameters. Both curves show an increase in the grain size in the region irradiated by the laser. Both curves also show that the maximum grain size does not occur at the joint interface. While the Monte Carlo model does slightly underpredict the grain size, the overall trend in the grain size as a function of position, as well as the strong agreement in the grain size between the simulation and experiments, suggests that the Monte Carlo model captures most of the physical processes responsible for grain growth during the Autogenous Laser Brazing process. It is important to remember at this point, however, that the Monte Carlo model does not account for grain annihilation due to melting. In reality, if the material under irradiation were to experience the thermal profiles predicted by the thermal model,

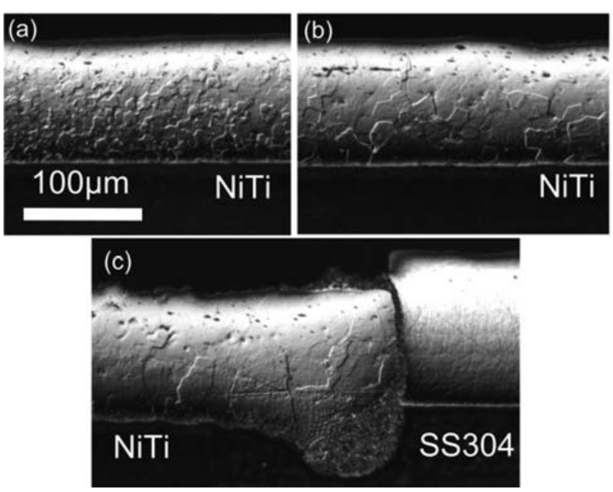

Fig. 8 Optical micrographs of typical tube wall cross section after mechanical polishing and chemical etching. Images taken (*a*) 2.5 mm away, (*b*) 1.2 mm away, and (*c*) at the dissimilar metal interface along the NiTi tube wall.

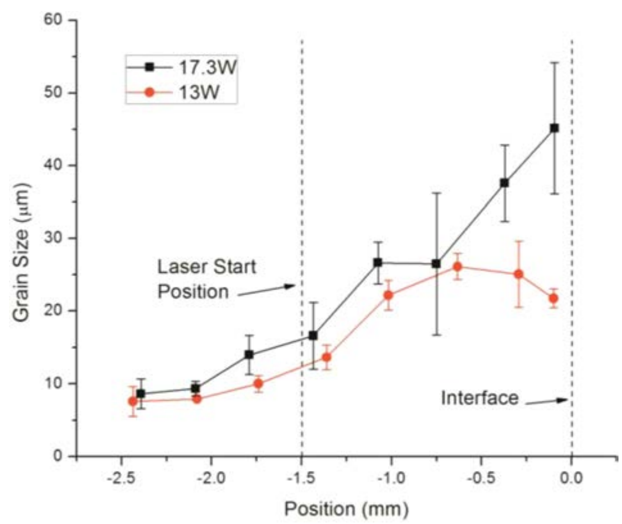

Fig. 9 Average grain size as a function of distance from joint interface as measured through line-intersect method on samples joined at two separate laser powers. Note decrease in grain size at interface for lower power.

regions would encounter a number of melting cycles before final solidification. Regions that experience melting and resolidification would not be expected to have a microstructure with any resemblance to the base material due to the unique thermal profile caused by localized laser irradiation. Thus, it is expected that the thermal model may currently overestimate the temperature in the irradiated region and that, experimentally, the temperature does not get over the melting temperature for the majority of the laser scan path.

The grain growth observed within the wall of the irradiated tubes also provides evidence as to the mechanism responsible for joining in this study. Grain size increases in a monotonic fashion from roughly the laser start point to a maximum some distance away from, or at, the interface. No sudden jumps in grain size, to larger or smaller grains, are observed along the path and grain sizes tend to the base material's grain size at the edge of the irradiated zone. These results suggest that little-to-no melting has occurred in these sections. If melting had occurred, the initial grain size of the base material would be erased, and due to the quick quenching provided by the localized thermal input of a laser beam and the minimal thermal mass of the tubing, a much finer grain size would be expected to form. Thus, initial evidence suggests that the autogenous laser brazing process, when applied to samples with a tubular geometry, results in primarily a diffusion-based joining mechanism. This is in contrast to the authors' previous work where it was found that for the joining of 381 μm diameter NiTi and SS wires, the joining was caused by localized melting at the joint interface.

Phase Identification. Figure 11(*a*) shows a grain map obtained through EBSD along the cross section of the joined sample, which was compositionally mapped in Fig. 3(*a*). Large grains are observed on the NiTi (left) side of the joint while small, equiaxed grains are observed in the stainless steel base material on the right side of the map. Between the two exists a region of columnar grains oriented parallel to the axis of the tubes with each grain spanning nearly the entire width of the joint. Figure 11(*b*) shows a phase map of the same region shown in Fig. 11(*a*). The leftmost and rightmost regions of the map are confirmed to consist of the NiTi and stainless steel base materials, respectively. Overall, it is observed that the different phases in the joint form in layers parallel to the original interface. The location of each phase is also observed to follow the trend predicted with increasing Fe content by the ternary Fe–Ni–Ti phase diagram going from the NiTi base material, through the joint, to the stainless steel. A NiTi/FeTi mixture, Ni_3Ti, and $TiFe_2$ are observed to form in succession across the joint.

When Fig. 11(*b*) is analyzed in terms of Fig. 11(*a*), it is noted that the grains within the joint consist of two phases, $TiFe_2$ and Ni_3Ti, in as much as their orientations, as depicted in Fig. 11(*a*), are indistinguishable. The $TiFe_2$ is observed to form predominantly on the stainless-steel side of the joint and the Ni_3Ti closer to the NiTi base material. A similar phenomenon is observed toward the NiTi base material. The phase map shows a mixed FeTi/NiTi layer adjacent to the NiTi base material which, as shown in Fig. 11(*a*), has the same orientation as the adjacent NiTi grain. In both of these cases, it is important to note that within both the $TiFe_2$/Ni_3Ti and FeTi/NiTi pairs, the two phases share the same crystallographic space group, which indicates that their levels and types of symmetry are identical. In addition, both FeTi and NiTi share the same CsCl-type structure with the conversion between the two phases only requiring substitution of a Fe atom for a Ni-atom or vice versa. In the $TiFe_2$/Ni_3Ti grains, this suggests that one of the phases formed after the other and formed at the same orientation as it provided a way to eliminate additional grain boundary energy. The columnar morphology of the grains also suggests the occurrence of directional growth during the joining process. It is interesting to note, however, that there is no observable orientation dependence between the columnar grains within the joint and either of the base materials.

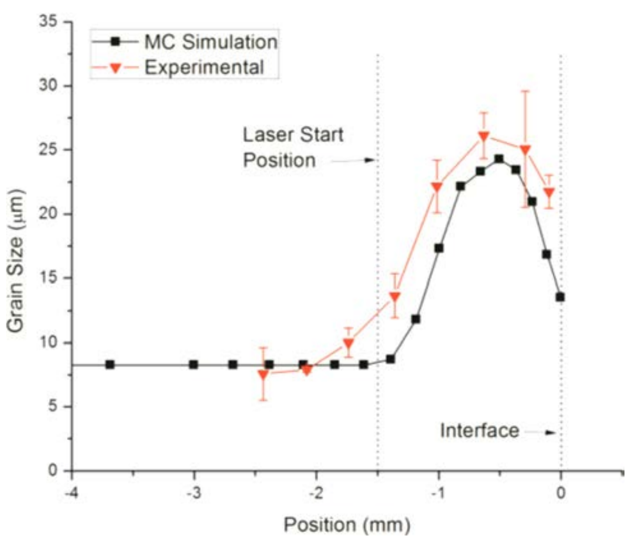

Fig. 10 Grain size as predicted by the Monte Carlo simulation and as measured experimentally for sample processed at 13 W power level. Note close agreement in grain size over laser scanned region.

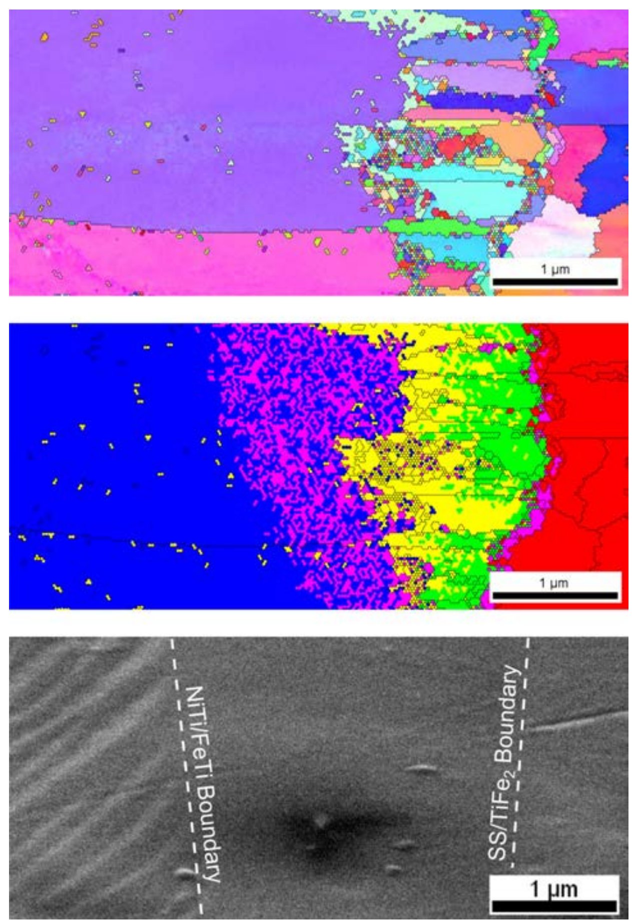

Fig. 11 (*a*) EBSD grain map with euler angle coloring. Note large grains on NiTi (left) side of joint, equiaxed grains on SS (right) side of joint, and columnar grains oriented along axial direction of tubes in the joint region. (*b*) Phase map of region shown in (*a*). Note formation of multiple phases in single grain regions.

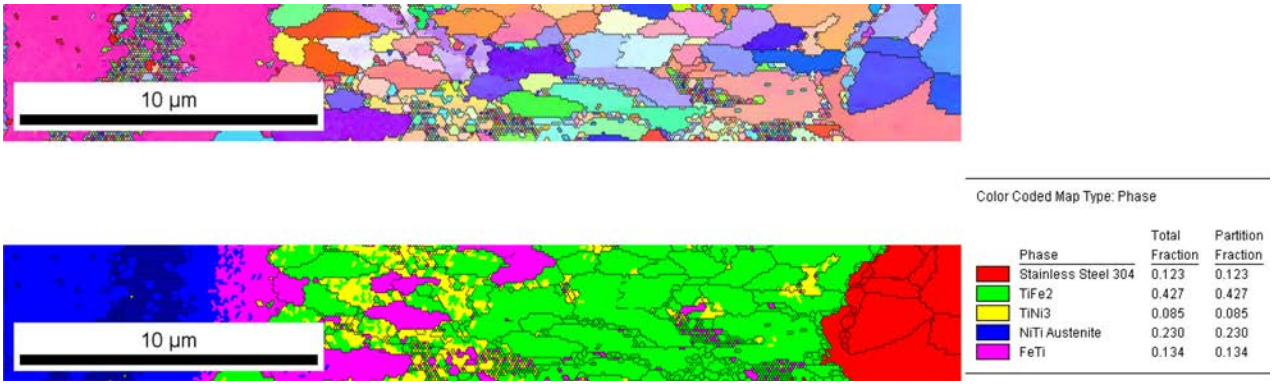

Fig. 12 (*a*) Grain map and (*b*) phase map of joint region for sample irradiated at laser power of 15.2 W. Note significantly greater joint width than observed in Fig. 11 and equiaxed grain geometry.

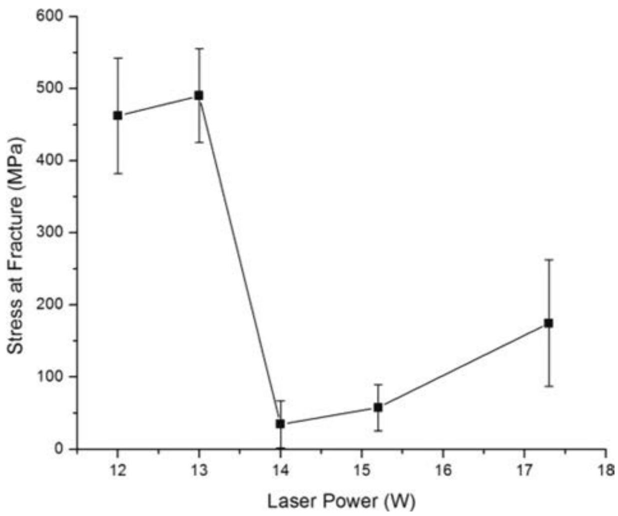

Fig. 13 Joint strength versus laser power. Note sharp drop in joint strength at 14 W.

Figure 11(*c*) shows an SEM image of the region mapped in Figs. 11(*a*) and 11(*b*). On the leftmost side of the image with only pure NiTi base material, surface relief indicative of martensite is observed. This surface relief is likely caused by the formation of a thin layer of martensite within the austenitic grains due to plastic deformation induced by the grinding and polishing process. The adjacent NiTi/FeTi region, however, does not show this surface relief despite the fact that the crystallographic orientation is the same and the material includes some NiTi. Thus, this mixed-phase region is not expected to exhibit shape memory properties. The formation of surface relief in the pure NiTi portions of those grains, however, suggests that this loss of shape memory properties will be limited to an exceedingly narrow layer, roughly 1 μm wide, along the joint.

Figures 12(*a*) and 12(*b*) show a grain map and a phase map for a sample irradiated at a higher power level whose composition profile was shown in Fig. 4(*b*). Processing at this higher power level was shown to form a wider joint, which is confirmed through the EBSD measurements. This portion of the joint is roughly 20 μm wide. A more significant difference between samples irradiated at low powers and high powers is observed, however, when considering the microstructure of the joint itself. At low powers, as shown in Fig. 11(*a*), the grains within the joint form a columnar geometry parallel to the tube axis. At a higher laser power as shown in Fig. 12(*a*), however, the grains within the joint are equiaxed, showing no evidence of directionality. In addition, multiple grains are observed to form across the joint's width in contrast to the single grains spanning the joint width in Fig. 11(*a*). The distribution of phases at high powers also shows some differences with a significantly higher percentage of the Fe-rich $TiFe_2$ phase compared to $TiNi_3$ due to the greater thermal input and resultant mixing between the base materials. Overall, the same phases are formed in both cases but are arranged in less uniform "layers" at higher laser powers. While intermetallic phases are observed to

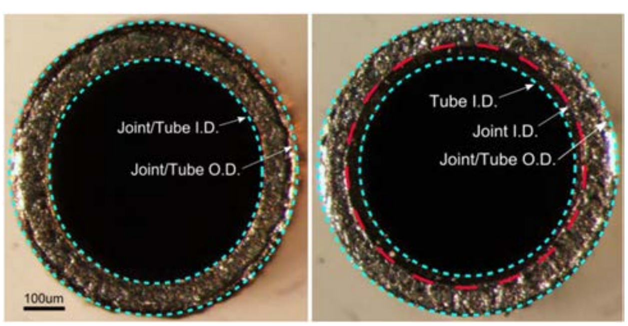

Fig. 14 Optical micrographs of fracture surface for sample processed at 13 W laser power. Note joining across entire NiTi tube wall (left) and a portion of the thicker SS tube wall (right) as indicated by tube and joint inner diameters (I.D.) and outer diameters (O.D.).

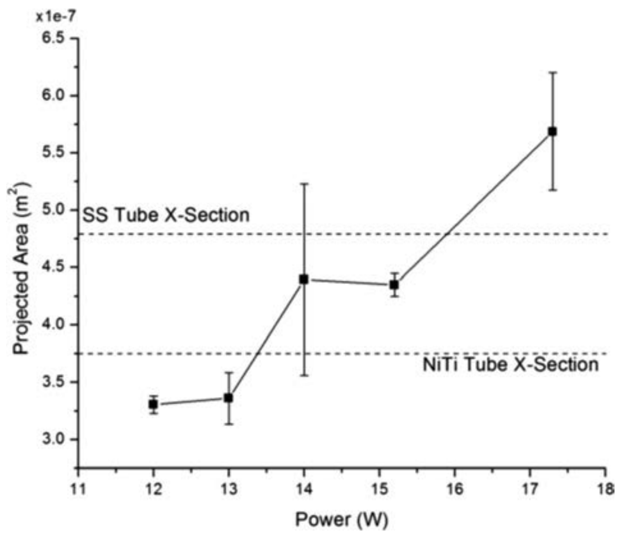

Fig. 15 Projected area of fracture surface as a function of laser power. Note small fracture area for low power irradiation and overmelting resulting in larger projected areas for high power irradiation.

form in both cases, it will be shown that the joint strength is a strong function of the joint width and uniformity.

Joint Strength. Figure 13 shows the strength of the joined samples measured in tension along the axis of the tubes for a range of applied laser powers, holding other parameters such as axial translation speed, laser spot overlap, axial force, and beam spot size constant. Due to differences in geometry for the samples irradiated at different laser powers, load at fracture values was normalized by the projected area of the fracture surface to determine the stress at fracture for each sample. Projected area is defined as shown in Fig. 14, with the results for various incident laser powers presented in Fig. 15. The joint strength is observed to be the highest and the most consistent at the lower power levels of 12 W and 13 W. As laser power is further increased to 14 W, a sharp drop in strength is observed which continues on to the samples irradiated at the 15 W power level. Joint strength increases slightly for the samples joined at the 17.3 W power level. While there seems to be little trend in the tensile strength results with power, these results can be better understood when they are considered in conjunction with the joint width and joint geometries discussed above. As observed in Figs. 3(*a*) and 3(*b*), the geometry of the joint is not uniform between different laser parameters. While the overall tubular shape of the members is maintained, higher laser powers show greater deformation and bulging in the joined region. At the highest laser powers, this causes the irradiated NiTi tube material to encompass the adjacent SS tube wall, which significantly increases the joining area and changes the joining geometry such that some regions are under tension and some under shear loading. While any increases in the projected area can be accounted for in the strength, increases in joining area under shear loading, caused by joining faced being perpendicular to the loading direction, are not included in the area calculation. It is believed that this increased joining area caused by the displaced NiTi material coming into contact with the inner and outer surfaces of the SS tube is responsible for the increased strength for the samples irradiated at the 17.3 W power level. The joints produced by the autogenous laser brazing process at the lower power levels show good strength with some reaching over 500 MPa in tension. In comparison, the base NiTi tube material undergoes a phase transformation between austenite and martensite at roughly 480 MPa. This phase transformation, however, was not observed during tensile testing. Figure 14 shows the NiTi and SS fracture surfaces from a joint formed at the 13 W power level (Fig. 15). The areas that were joined before fracture can be identified by their brighter appearance and lack of oxidation-induced discoloration. The joining between the NiTi and SS tubes at low power was limited to a cross section roughly the size of the NiTi tubes cross section as shown by the greater joint inner diameter (I.D.) relative to the tube I.D. on the stainless side. At higher power levels, the joint was observed to encompass a much larger cross-sectional area than either the NiTi or SS tube cross sections. This is enabled by the excessive deformation of the tubes during joining causing them to collapse and lose their shape. As shown in Fig. 11, which

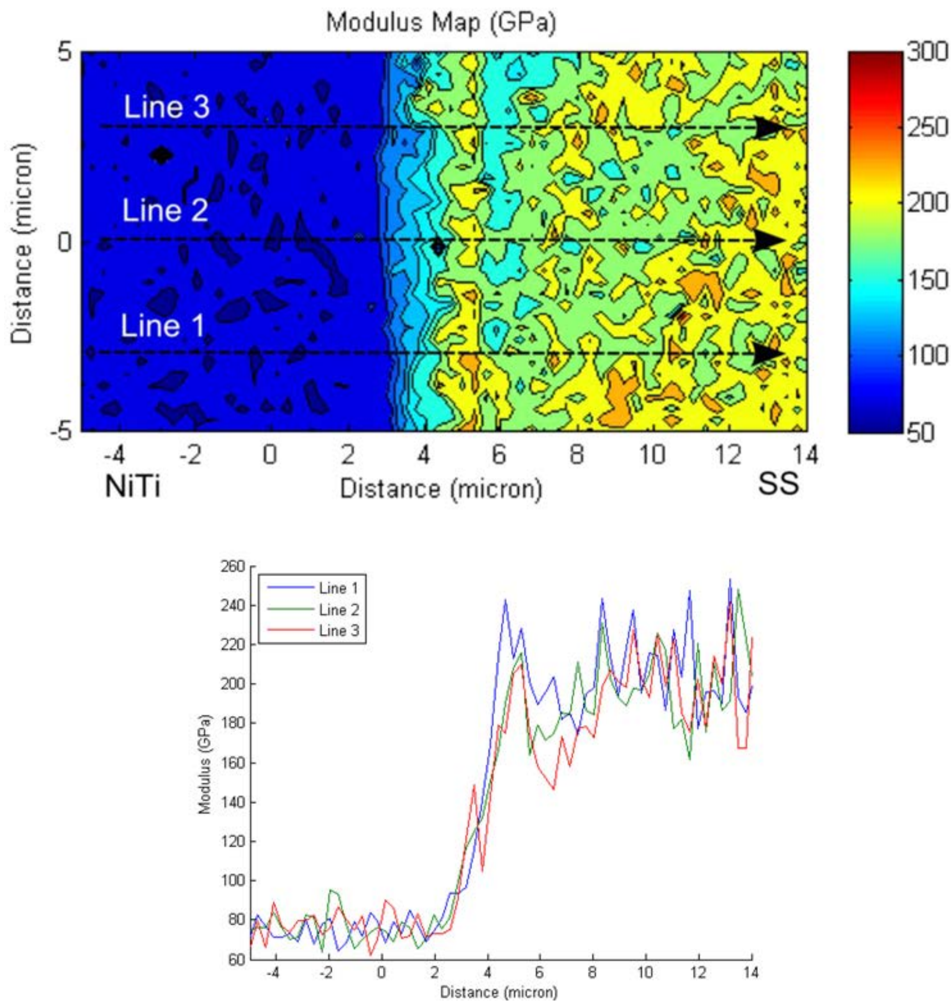

Fig. 16 Modulus (*a*) map and (*b*) line profiles of a localized region around the joint for a sample irradiated at a laser power of 13 W. Note similarity between modulus of stainless steel base material and intermetallics within the joint.

depicts the projected cross-sectional area after fracture as a function of laser power, the joint area for the samples irradiated at low powers is actually smaller than the original NiTi cross section. This difference between the joint cross section and the base material's causes the stress in the NiTi to be lower than at the joint, causing the phase transformation not to occur. At the higher power levels, the joining area is greater than both the base materials; however, the overall strength is too low to cause the phase transformation to occur in the NiTi tube.

The overall trend of reduction of strength as a function of laser power can be explained through the microstructure and thickness of the mixed layer formed between the two base materials. As shown in Fig. 5, the width of the joint increases with power due to the greater temperature achieved and resultant greater mixing between the materials. While the thickness of the joint may seem inconsequential, the brittle nature of the intermetallic phases that can form in a NiTi–SS mixture causes it to be an important consideration. Since brittle fracture is the expected failure mechanism in such materials, the failure stress is a function of the fracture toughness and the initial crack size. As the dimensions of the mixed layer decrease, so does the maximum initial crack size which leads to a higher fracture strength. Wei et al. have shown similar results for the tensile strength of Aluminum–Copper joints with intermetallic layer thickness [15].

Another goal of the autogenous laser brazing process is to create microstructures within the joints that are less susceptible to brittle fracture. While Fig. 5 shows that the overall width of the joints increases with laser power, the microstructure within the mixed layer could be any combination of phases with different thicknesses. The authors have shown that joining between NiTi and SS with a melt-dominated process results in a near-homogenous composition across the mixed layer due to the strong mixing due to diffusive and convective mass transport. The composition profiles shown in Fig. 4, however, only show constant composition mixed layers to form at higher laser powers. At the low laser powers such as in Fig. 4(*a*), the composition is seen to vary smoothly and monotonically from one base material to the other, indicative of a diffusion-dominated mechanism. While the effect of varying laser power has been focused on here, a description of the influence that rotation speed has on laser autogenous brazing can be found in an additional publication by the authors [16].

Spatially Resolved Material Characterization. Spatially resolved characterization of the joint and the adjacent base materials is performed through nanoindentation mapping. Samples are loaded under a Berkovich indenter tip at a spacing of 300 nm to a

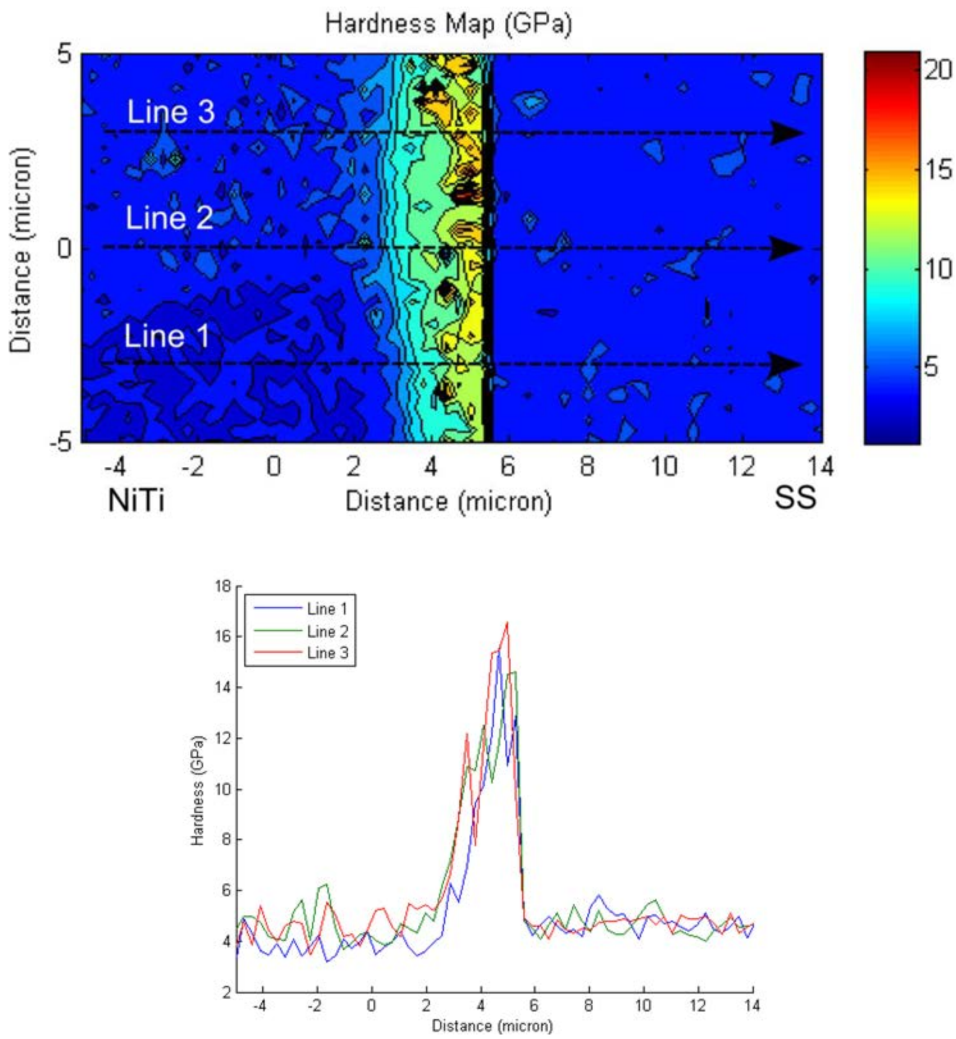

Fig. 17 Hardness (*a*) map and (*b*) line profiles of a localized region around the joint for a sample irradiated at a laser power of 13 W. Note intermetallics are significantly harder than either of the base materials and gradual change from level of base NiTi to that of intermetallics and steep gradient on stainless steel side.

maximum load of 0.4 mN. Figures 16(*a*) and 16(*b*) show a modulus map and line profiles about the joint for a sample irradiated at a low power level of 13 W. The modulus map clearly captures the variation in material properties between the two base materials. The NiTi base material has a modulus of roughly 70 GPa and the stainless steel 200 GPa. Between the two base materials, the layers of intermetallic phases result in a gradient in modulus, which shows an increasing trend going from the NiTi to the stainless sides of the joint. The modulus of the $TiFe_2$ intermetallic is nearly the same as the stainless steel base material and thus the interface between the joint material and the stainless steel cannot be easily discerned.

The hardness map and line profile shown in Fig. 17, however, show significant differences between the materials with the intermetallics having the highest hardness. A gradient in hardness is also observed across the width of the joint, increasing toward the stainless steel side of the joint. The hardness of the base stainless steel, however, is significantly lower than the adjacent $TiFe_2$ layer, which results in a clearly defined boundary. The hardness changes more gradually on the NiTi side of the joint, which is expected considering the greater amount of diffusion occurring on within the irradiated tube. As shown in Fig. 11 above, the phase interfaces are more diffuse on the NiTi side of the joint. The width of the joint as observed from the hardness map is very similar to that observed experimentally through optical imaging and EBSD with the inclusion of the FeTi layer. It is interesting, however, to note that the layer of FeTi observed on the NiTi side of the joint does show significantly different material properties to the base NiTi material. It was observed through SEM imaging that, while the two phases existed within the same grain, the surface relief indicative of shape memory properties was lacking in the FeTi region. This gives us an estimate of what distance away from the interface the material properties are changed from that of the base NiTi material. Overall, we see that a narrow region roughly 1 μm wide at the interface exhibits properties, which vary from the NiTi base material. This corresponds well to the width of the NiTi/FeTi layer identified through EBSD.

Figures 18(*a*) and 18(*b*) show a modulus map and line profile for a sample irradiated at a higher power level of 15.2 W. As shown in Fig. 3 above, this results in greater deformation at the interface and a wider joint. Unlike the modulus map for the sample irradiated at 13 W shown in Fig. 16, a gradient in modulus is not formed for the higher power level. This is consistent with the greater mixing between the intermetallic phases for samples irradiate at higher power levels. The greater joint width as observed through EBSD is confirmed by the hardness map which shows a region roughly 20 μm wide with increased hardness. A slight gradient is observed across the joint, increasing toward the stainless steel side of the joint, which is most apparent in the two-dimensional map.

Measurements of fracture toughness can also be performed in a spatially resolved manner using nanoindentation. Figure 19 shows the residual indentation impression performed using a cube-corner indenter tip on a sample irradiated at the lower power level of

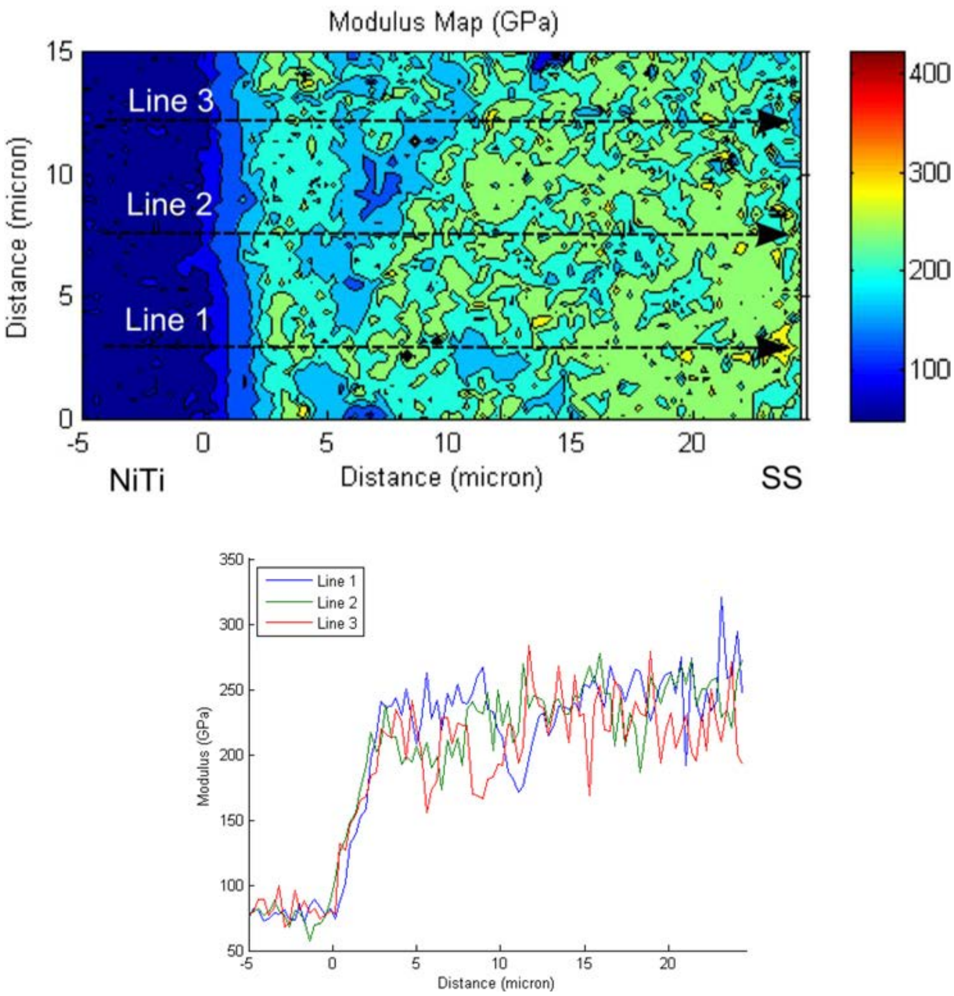

Fig. 18 Modulus (*a*) map and (*b*) line profile for a sample irradiated at a laser power of 15.2 W. Note the large joint width when compared to that shown in Fig. 16. Modulus of intermetallics is again similar to that of the stainless steel. Gradient is observed toward NiTi side of joint.

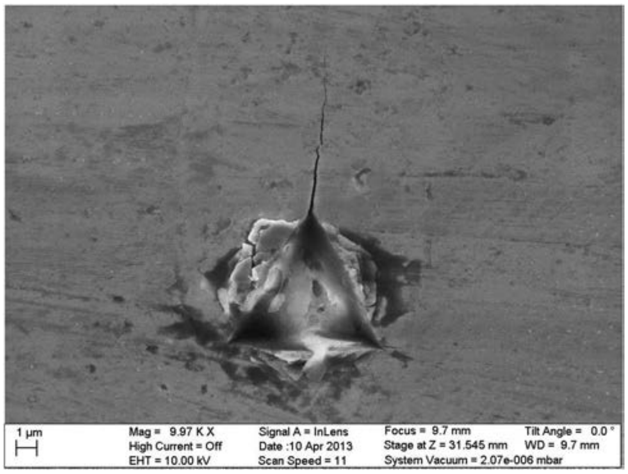

Fig. 19 Scanning electron microscope image of indentation performed within joint of sample irradiated at laser power level of 13 W. Note primary radial crack extending upward from one corner of indentation. Significantly smaller cracks are observed on the other two corners.

13 W. Some pileup of material around the indentation is observed which is due to plastic deformation. Cracking is observed around the indentation with a long primary radial crack observed to form from the top corner of the indentation impression. The other two corners of the indentation show much smaller radial crack lengths. This variability in crack lengths can be understood in terms of the joint geometry. Figure 20 shows an optical micrograph of the same indentation showing the width of the joint in which the indentation was placed, and the relative orientation of the tip. The uppermost corner of the indenter is oriented such that the stress concentration at the corner applies a stress directly perpendicular to the joint surface. This produces the long radial crack which propagates along the joint plane. The other two corners of the indenter result in cracks which are directed toward the two base materials. The base materials are significantly more ductile than the intermetallics within the joint which result in blunting of the crack tips and significantly shorter crack lengths. The fracture toughness of the material within the joint, based on the single, long crack, is calculated to be roughly 1.5 MPa($m^{1/2}$). An SEM image of an indentation performed within the larger joint formed within samples irradiated at a laser power of 15.2 W is shown in Fig. 21. Rather than primary radial cracks, however, only secondary radial cracks are observed. As the highest stress

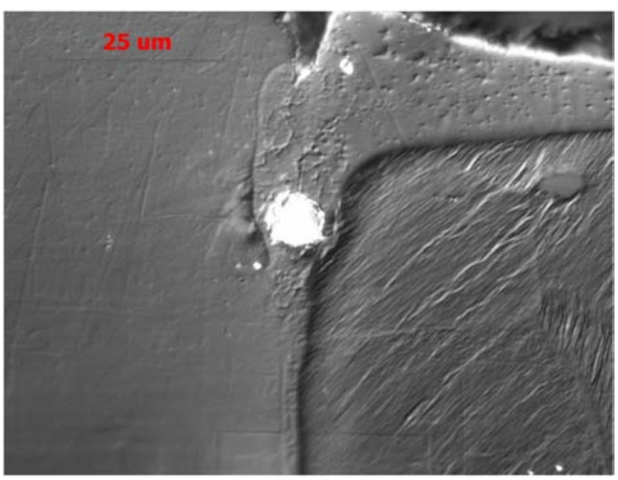

Fig. 20 DIC optical micrograph of indentation shown in Fig. 21. Note location of indentation within joint and proximity of lower corners to base materials which blunt crack growth.

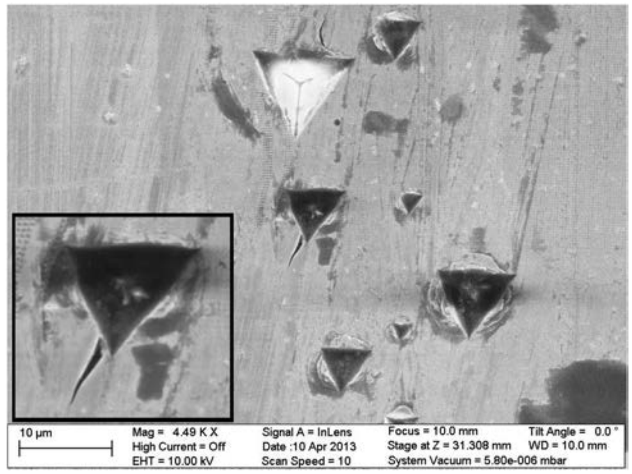

Fig. 21 SEM image of indentations performed within joint for sample irradiated at laser power of 15.2 W. Note lack of primary radial cracks and single secondary radial crack initiated at edge of indentation impressions (inset).

concentrations under the indenter tip are located at the corners of the indentation, the formation of secondary radial cracks, which form on the flat edges of the indentation impression, requires a locally lower fracture toughness at that location. This is most likely due to the highly anisotropic nature of the hexagonal intermetallics formed within the joint. The preferred cleavage plane for hexagonal materials is the (0001) basal plane. The size of the indentation, at roughly 4 μm across, covers multiple grains of different orientations as shown in the EBSD map in Fig. 12. As the stress field develops around the indenter, grains with orientations which result in the greatest stress on this cleavage plane fracture first.

Figures 22(*a*) and 22(*b*) show the modulus over hardness ratio for the samples described in Figs. 16 and 17 above. The modulus

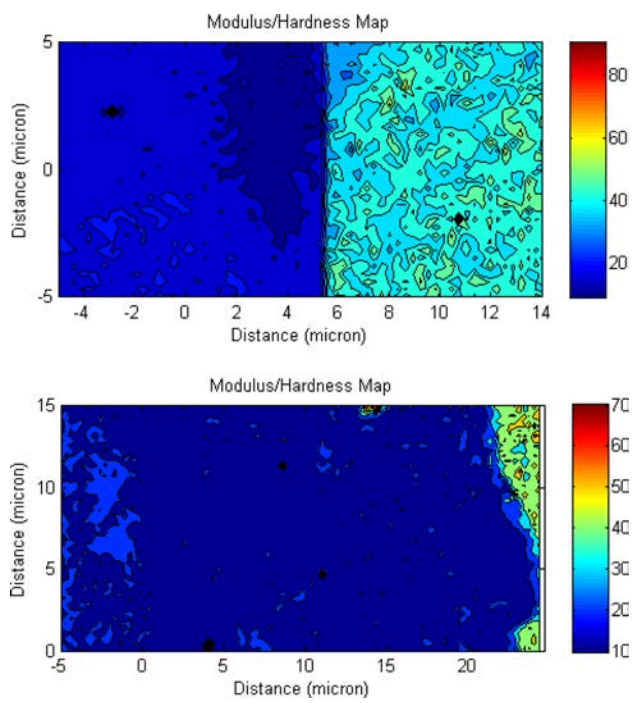

Fig. 22 Modulus over hardness maps for the samples shown in Figs. 16 and 18 above. Note the uniformity of the *E/H* ratio in the NiTi and joint regions. This suggests that the residual stress field surrounding the indenter, which is responsible for radial crack growth, is the same between the two materials.

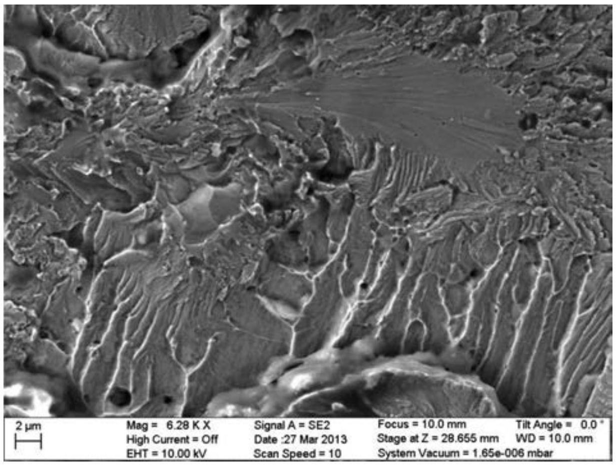

Fig. 23 Representative fracture surface for sample irradiated at low laser power of 13 W. Surface shows features indicative of quasi-cleavage fracture.

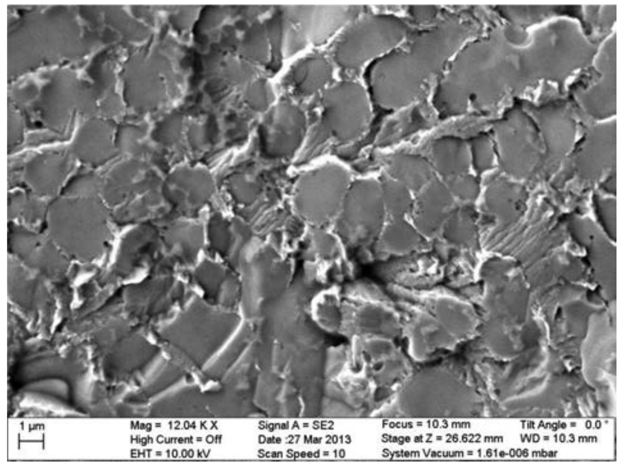

Fig. 24 Representative fracture surface for sample irradiated at high laser power of 15.2 W. Note surface morphology indicative of transgranular fracture. Multiple grains are observed in the in-plane direction.

over hardness ratio, which has a strong effect on the fracture toughness as seen in Eq. (5), of the intermetallic phases within the joint is nearly identical to that of the NiTi base material, both of which are lower than that of the stainless steel base material. As the E/H term in Eq. (4) describes the strength of the residual stress field left by the plastically deformed material under the indentation and is proportional to the maximum crack opening force, the properties of the intermetallics themselves do not result in higher stresses under indentation loading. Rather, the lower fracture toughness of the intermetallics within the joint result in fracture occurring within the joint.

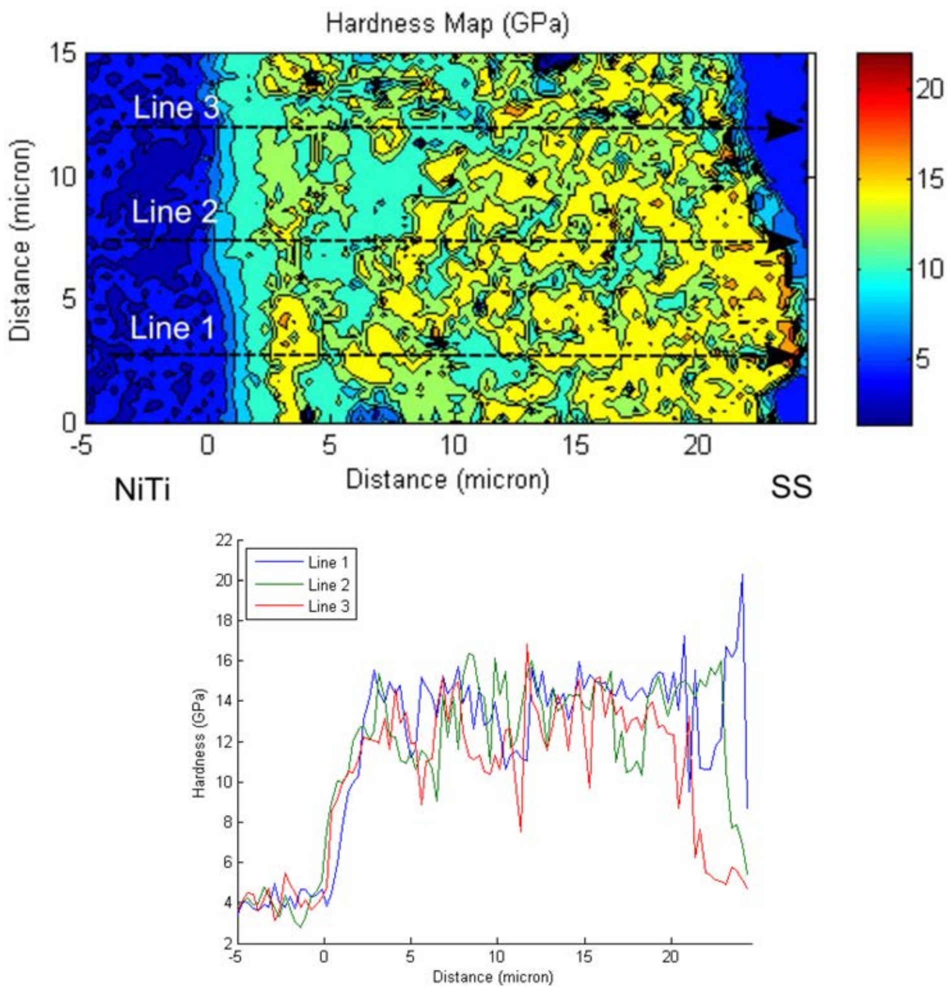

Fig. 25 Hardness (*a*) map and (*b*) line profile for a sample irradiated at a laser power of 15.2 W. Hardness line profiles show greater uniformity of hardness across joint than that observed for samples irradiated at lower power level of 13 W (Fig. 17).

Fracture Surface. Figure 23 shows a fracture surface representative of that observed on samples irradiated at lower power levels obtained from scanning electron microscopy. The fracture surface itself is indicative of quasi-cleavage fracture. A feather pattern is observed in the upper portion of the image, a feature corresponding to brittle transgranular fracture. Toward the lower half of the image, however, features are observed which are consistent with ductile tearing. These features are seen to transition directly into cleavage fracture facets. This overall morphology is described as quasi-cleavage fracture. As shown above in Fig. 13, samples irradiated at lower power levels, which exhibit quasi-cleavage fracture surfaces, show high strength values.

Figure 24 shows a representative fracture surface image obtained through SEM of a sample irradiated at a higher power level. The fracture surface morphology is significantly different than that observed for the lower laser power samples shown in Fig. 25. At the higher power levels, evidence of intragranular fracture is observed with multiple grains observed to intersect the crack surface. Roughly, circular features are observed on the fracture surface that is roughly 2 μm in diameter. These circular sections are believed to be the grains formed within the dissimilar metal joint. The size of the circular regions agrees well with the grain size in the radial direction as seen through EBSD as shown in a sample irradiated with identical parameters shown in Fig. 12.

It is important to note that the interface formed at higher laser powers has a structure consisting of multiple grains spanning the joint width. The larger joint width compared to the samples irradiated at lower laser powers results in a larger volume of brittle intermetallic material at the interface. Since cleavage is observed to occur on (0001) planes in hexagonal crystals, the $TiFe_2$ and Ni_3Ti phases formed at the interface both have a hexagonal structure. The formation of multiple grains within the joint results in a greater variety of crystallographic orientations to form, increasing the probability that a (0001) plane will be oriented perpendicular to the loading direction. Cracks forming within this region are also able to travel larger distances without encountering the ductile base materials. In contrast, for thinner joints, the joints consist of an intermetallic layer, that is, one grain thick. This results in less avenues for crack propagation through the intermetallic and the resulting quasi-cleavage fracture morphology.

Conclusion

The use of autogenous laser brazing, a new process for joining dissimilar metals without filler materials, has been investigated for the joining of 1 mm diameter NiTi and stainless steel tubes. Joint strengths achieved using this process reach 500 MPa, approaching the phase transformation stress of the NiTi base material as well as the tensile strength of soft temper stainless steel. Joints created through this process do not encroach on the lumen of the tubes, which is critical for the intended medical device applications. Line-scan EDS profiles show that joint widths are a strong function of applied laser power, while holding constant the spot size and scan speed, with the thinnest joints having a width of less than 10 μm. Sequentially coupled finite element thermal and Monte Carlo grain growth simulations suggest that the joining mechanism for tubes is diffusion-based rather than the melt-dominated mechanism observed in a previous study by the authors on joining NiTi and Stainless Steel wires.

Acknowledgment

The authors acknowledge financial support from NSF under GOALI Award CMMI-1130564. Use of characterization equipment in the Shared Materials Characterization Laboratory, Columbia University, is gratefully acknowledged.

References

[1] Sun, Z., and Ion, J. C., 1995, "Review Laser welding of Dissimilar Metal Combinations," J. Mater. Sci., **30**(17), pp. 4205–4214.
[2] Springer, H., Kostka, A., Payton, E. J., Raabe, D., Kaysser-Pyzalla, A., and Eggeler, G., 2011, "On the Formation and Growth of Intermetallic Phases During Interdiffusion Between Low-Carbon Steel and Aluminum Alloys," Acta Mater., **59**(4), pp. 1586–1600.
[3] Matsuoka, S., and Imai, H., 2009, "Direct Welding of Different Metals Used Ultrasonic Vibration," J. Mater. Process. Technol., **209**(2), pp. 954–960.
[4] Watanabe, T., Sakuyama, H., and Yanagisawa, A., 2009, "Ultrasonic Welding Between Mild Steel Sheet and Al–Mg Alloy Sheet," J. Mater. Process. Technol., **209**(15–16), pp. 5475–5480.
[5] Ghosh, M., and Chatterjee, S., 2002, "Characterization of Transition Joints of Commercially Pure Titanium to 304 Stainless Steel," Mater. Charact., **48**(5), pp. 393–399.
[6] Kundu, S., and Chatterjee, S., 2008, "Characterization of Diffusion Bonded Joint Between Titanium and 304 Stainless Steel Using a Ni Interlayer," Mater. Charact., **59**(5), pp. 631–637.
[7] Campbell, C. E., and Boettinger, W. J., 2000, "Transient Liquid-Phase Bonding in the Ni-Al-B System," Metall. Mater. Trans. A, **31**(11), pp. 2835–2847.
[8] Vannod, J., Bornert, M., Bidaux, J.-E., Bataillard, L., Karimi, A., Drezet, J.-M., Rappaz, M., and Hessler-Wyser, A., 2011, "Mechanical and Microstructural Integrity of Nickel–Titanium and Stainless Steel Laser Joined Wires," Acta Mater., **59**(17), pp. 6538–6546.
[9] Satoh, G., and Yao, Y. L., 2011, "Laser Autogenous Brazing—A New Method for Joining Dissimilar Metals," 30th International Congress on the Applications of Lasers and Elecro-Optics, Lake Buena Vista, FL, pp. 315–324.
[10] Wagner, C., 1969, "The Evaluation of Data Obtained With Diffusion Couples of Binary Single-Phase and Multiphase Systems," Acta Metall., **17**(1), pp. 99–107.
[11] Bader, S., Gust, W., and Hieber, H., 1995, "Rapid Formation of Intermetallic Compounds by Interdiffusion in the Cu-Sn and Ni-Sn Systems," Acta Metall. Mater., **43**(1), pp. 329–337.
[12] Pharr, G. M., Harding, D. S., and Oliver, W. C., 1993, "Measurement of Fracture Toughness in Thin Films and Small Volumes Using Nanoindentation Methods," *Mechanical Properties and Deformation Behavior of Materials Having Ultra-Fine Microstructures* (NATO Science Series), Vol. 233, M. Nastasi, D. M. Parkin, and H. Gleiter, eds., Springer, The Netherlands, pp. 449–461.
[13] Satoh, G., Huang, X., Ramirez, A. G., and Lawrence Yao, Y., 2012, "Characterization and Prediction of Texture in Laser Annealed NiTi Shape Memory Thin Films," ASME J. Manuf. Sci. Eng., **134**(5), p. 051006.
[14] Raabe, D., 2000, "Scaling Monte Carlo Kinetics of the Potts Model Using Rate Theory," Acta Mater., **48**(7), pp. 1617–1628.
[15] Wei, X., Yamaguchi, T., and Knishio, K., 2011, "Formation of Intermetallic Compounds on the Bond Interface of Aluminum-Clad Copper and Its Influence on Bond Tensile Strength," Appl. Mech. Mater., **117–119**, pp. 984–989.
[16] Brandal, G., Satoh, G., Yao, Y. L., and Naveed, S., 2013, "Beneficial Interface Geometry for Laser Joining of NiTi to Stainless Steel Wires," ASME J. Manuf. Sci. Eng., **135**(6), p. 061006.